RSC Advances

ROYAL SOCIETY OF CHEMISTRY

PAPER

View Article Online
View Journal | View Issue

Cite this: *RSC Adv.*, 2025, **15**, 28626

Green synthesis of *Aloe vera*-assisted Co_3O_4 nanostructures: structural, electronic, optical, and electrochemical insights for supercapattery applications

Mohit Bhatt, *[a] Kajal Gautam, [b] Payal Dhyani[c] and A. K. Sinha*[a]

Received 22nd May 2025
Accepted 7th August 2025

DOI: 10.1039/d5ra03604f

rsc.li/rsc-advances

Green synthesis is an emerging and sustainable approach for developing functional nanomaterials using environmentally benign resources. In this work, cobalt oxide (Co_3O_4) nanostructures were successfully synthesized *via* a green synthesis, employing *Aloe vera* gel as a natural reducing and stabilizing agent. This phytochemical-assisted synthesis eliminates the need for hazardous chemicals and offers a cost-effective, eco-friendly alternative for nanomaterial fabrication. The resulting Co_3O_4 exhibited a phase-pure spinel structure with an average crystallite size of ~32 nm, as confirmed by synchrotron X-ray diffraction (XRD), and showed excellent thermal stability with only 3.5% weight loss up to 750 °C (TGA). FTIR analysis revealed strong Co–O stretching vibrations along with *Aloe vera*-derived surface functionalities, indicating successful templating and stabilization. X-ray photoelectron spectroscopy (XPS) confirmed the coexistence of Co^{2+}/Co^{3+} oxidation states, surface hydroxyls, and chemisorbed oxygen features that contribute to a redox-active, defect-rich surface. X-ray absorption spectroscopy (XAS) further supported these findings by revealing oxidation state distribution, crystal field splitting, and strong Co–O hybridization. Additionally, UV-Vis spectroscopy showed a direct band gap of 3.65 ± 0.10 eV, suggesting good electronic quality with low intrinsic defect density. Electrochemical studies demonstrated excellent performance, with specific capacitance values of 450.7 F g^{-1} at 1 mV s^{-1} and 467.9 F g^{-1} at 0.5 A g^{-1}, along with outstanding cycling stability (83% retention) and 100% coulombic efficiency after 3000 cycles at 10 A g^{-1}. These results highlight the synergistic contributions of green synthesis and intrinsic structural-electronic properties, establishing *Aloe vera* assisted Co_3O_4 as a promising electrode material for supercapattery applications.

1. Introduction

Green synthesis is becoming increasingly vital in nanotechnology due to growing environmental concerns and the urgent need to develop sustainable, eco-friendly alternatives to conventional chemical processes.[1] Traditional synthesis methods often rely on hazardous reagents, high energy consumption, and generate toxic by-products that pose significant risks to human health and the environment.[2,3] In contrast, green synthesis utilizes biological materials, such as plant extracts, microorganisms, and biopolymers as reducing, stabilizing, and capping agents, eliminating the need for harmful chemicals.[1,4] This approach not only aligns with the principles of green chemistry but also offers simplicity, low cost, biocompatibility, and scalability.[2,5] In recent years, green synthesis has been widely adopted for the fabrication of metal and metal oxide nanostructures, owing to its potential to produce stable and functional materials with tailored properties under mild reaction conditions.[4–6]

Transition metal oxides (TMOs) derived from conventional synthetic methods often face several disadvantages, including high energy consumption, use of hazardous reagents, generation of toxic by-products, and limited control over surface chemistry and morphology.[7] These processes typically require prolonged reaction durations (often 12–24 hours) at elevated temperatures (>180 °C), involve corrosive solvents or surfactants, and frequently necessitate multiple washing and purification steps, contributing to environmental risk and increased production cost.[7,8] In contrast, green synthesis approaches utilizing plant extracts significantly reduce processing temperature and duration, while eliminating the need for toxic chemicals. For instance, plant-based reducing agents like flavonoids and polyphenols act simultaneously as chelating, stabilizing, and templating agents, leading to improved

---

[a] *Department of Physics, School of Advanced Engineering, UPES, Dehradun, India. E-mail: mhtt.mb@gmail.com; anilksinha11@gmail.com*

[b] *Department of Chemistry, School of Advanced Engineering, UPES, Dehradun, India*

[c] *Division of Genetics & Tree Improvement, ICFRE-Forest Research Institute, Dehradun, India*

material properties and eco-friendly processing.[9] Preliminary comparative studies suggest that green methods can reduce chemical cost and energy input by 30–40% compared to hydrothermal or solvothermal synthesis routes.[10] Thus, green synthesis not only aligns with sustainability goals but also offers a scalable, cost-effective pathway for fabricating high-performance nanomaterials. Numerous studies have explored the green synthesis of metal oxides using plant-based extracts, which are rich in bioactive compounds like flavonoids, polyphenols, alkaloids, terpenoids, and sugars.[1,2,5,11–13] These biomolecules play a crucial role in reducing metal ions and stabilizing the resulting nanostructures. For instance, ZnO nanoparticles have been synthesized using *Aloe vera gel extract*, *Moringa oleifera*, *Azadirachta indica*, and *Camellia sinensis* extracts;[9,14–16] TiO_2 has been prepared using *Ocimum sanctum* (holy basil) and *Eucalyptus globulus*;[17,18] NiO, CuO and Fe_3O_4 nanoparticles have been synthesized using *Punica granatum*,[19] *Allium sativum*,[20] and *Acalypha indica*[21] respectively. These green-synthesized nanomaterials have shown promising performance in applications such as photocatalysis, antimicrobial coatings, sensors, and energy storage applications. Among the various biological agents used for green synthesis, *Aloe vera* has emerged as a particularly attractive option due to its rich phytochemical profile, which includes flavonoids, phenolic acids, saponins, amino acids, and polysaccharides, which serve multiple chemical functions during nanoparticle formation.[22–24] These bioactive molecules act not only as reducing agents for converting metal precursors into oxide forms, but also as stabilizers and morphology-directing agents that govern particle size and shape.[22] *Aloe vera* has already been employed in the green synthesis of oxide nanostructures such as NiO, ZnO, and CuO, demonstrating excellent morphology control, biocompatibility, and functional properties.[4,15,20] In contrast, green synthesis using natural plant extracts such as *Aloe vera* offers an eco-friendly and efficient alternative, with better control over surface functionalities. *Aloe vera* induces surface functional groups like –O–C=O and oxygen vacancies, which are well-documented in the literature to improve wettability and enhance specific capacitance.[9,12] However, despite its potential, limited studies have focused on *Aloe vera*-assisted synthesis of Co_3O_4, especially for electrochemical energy storage in supercapattery applications.

Cobalt oxide (Co_3O_4) is a p-type transition metal oxide with a spinel structure that has garnered considerable interest due to its excellent redox activity,[25,26] high theoretical capacitance ($\sim$3560 F g^{-1}), good electrical conductivity, and chemical stability.[26,27] It has been widely used in catalysis, gas sensors, lithium-ion batteries, and supercapacitors.[26,28] However, the synthesis route plays a critical role in determining its morphology, crystallinity, surface area, and electrochemical performance.[18,20] In energy storage applications, particularly for supercapatteries (which combine the fast charge–discharge capability of supercapacitors with the high energy density of batteries),[29,30] Co_3O_4 can serve as a highly promising electrode material when synthesized with suitable nanostructuring and surface features.[31,32] Energy storage devices are crucial in the current era of renewable energy, especially to bridge the gap between energy production and demand.[3,33] Non-conventional sources like solar and wind produce electricity intermittently, only when sunlight or wind is available, leading to mismatches between generation and consumption.[3,34] To effectively utilize these sources, high-performance energy storage systems are needed that can store excess energy and supply it when needed. Various materials, such as carbonaceous structures, metal oxides, sulfides and hydroxides, have been studied to meet this demand.[35,36]

In the present work, we report the green synthesis of Co_3O_4 nanostructures using *Aloe vera* extract as a multifunctional biogenic reducing, chelating, and stabilizing agent.[12,23] *Aloe vera* plays a critical role in directing the synthesis process through its rich phytochemical profile, including flavonoids, phenols, saponins, carboxylic acids, and amino acids.[9] These compounds act as natural chelating agents, enabling uniform dispersion of Co^{2+} ions in aqueous medium, while simultaneously functioning as bio-templates during gel formation, guiding the nucleation and growth of Co_3O_4 crystals into porous nanostructures.[9,12] Additionally, they act as surface stabilizers, preventing nanoparticle agglomeration and enhancing structural uniformity. Upon calcination, the bio-organics decompose cleanly, promoting surface porosity and exposing redox-active sites critical for improved electrochemical behavior. In a recently reported study, a transition metal oxide (TMO), ZnO, was successfully synthesized using *Aloe vera* gel extract, where the phytochemical constituents such as flavonoids, phenolic acids, amino acids, and polysaccharides played a vital role in controlling nucleation, crystal growth, and surface stabilization of the nanostructures.[9] These naturally derived compounds acted as reducing, chelating, and capping agents, facilitating the formation of ZnO with desirable morphological and functional properties.[9] Building upon this approach, the present work applies *Aloe vera* extract in the green synthesis of Co_3O_4 nanostructures, leveraging its multifunctional role to direct crystal growth, prevent agglomeration, and enhance redox-active surface development. Despite the known benefits of *Aloe vera*-assisted synthesis in other oxide systems, its application to Co_3O_4 for electrochemical energy storage remains largely unexplored. This study addresses this gap by demonstrating an environmentally benign and effective approach for fabricating Co_3O_4 nanostructures with impressive electrochemical performance. A comprehensive investigation was conducted on the synthesized *Aloe vera-assisted* Co_3O_4 (*Alv-Co₃O₄NSs*) nanostructures, including synchrotron-based X-ray diffraction (XRD) for structural analysis, X-ray absorption spectroscopy (XAS) for probing electronic states, X-ray photoelectron spectroscopy (XPS) for possible oxidation state, SEM and TEM for morphological examination, and UV-Vis and thermogravimetric analysis (TGA) to assess optical and thermal properties. The electrochemical performance was thoroughly evaluated using cyclic voltammetry (CV), galvanostatic charge–discharge (GCD), and electrochemical impedance spectroscopy (EIS) to establish a strong correlation between material properties and energy storage behaviour. This work demonstrates the potential of *Aloe vera* as a green and effective synthesis medium for developing high-performance electrode materials in a sustainable and environmentally responsible manner for supercapattery applications.

2. Experimental section

2.1. Characterization techniques

The synthesized *Aloe vera*-assisted Co_3O_4 nanostructures (*Alv-Co_3O_4 NSs*) were characterized using a range of analytical techniques to understand their structural, morphological, and thermal properties. X-ray Diffraction (XRD) was employed to determine the crystal structure and phase purity of the material. Fourier Transform Infrared Spectroscopy (FTIR) was used to identify functional groups and confirm the presence of *Aloe vera*-derived organic moieties. Thermogravimetric analysis (TGA) was carried out to assess the thermal stability and decomposition behaviour. Field Emission Scanning Electron Microscopy (FESEM) revealed the surface morphology of the nanostructures, while Energy Dispersive X-ray Spectroscopy (EDX) confirmed their elemental composition. Transmission Electron Microscopy (TEM) was conducted to investigate the particle size and internal lattice arrangements.

2.2. Synthesis of Co_3O_4 nanostructures (*Alv-Co_3O_4 NSs*)

Fresh *Aloe vera* leaves were collected from the polyhouse at UPES, Dehradun, and thoroughly rinsed with deionized water to eliminate surface impurities. Approximately 20 g of *Aloe vera* gel was extracted from the leaves and blended with 100 mL of deionized water to form a homogenous, viscous solution. This mixture was then subjected to mild heating at 85 °C for 2 hours in a hot air oven to facilitate the release of bioactive compounds. Separately, 10 g of cobalt nitrate hexahydrates ($Co(NO_3)_2 \cdot 6H_2O$) was dissolved in the prepared *Aloe vera* gel under constant stirring. The *Aloe vera* extract served as both a reducing and stabilizing agent, facilitating the uniform dispersion of cobalt ions. The resulting mixture was continuously stirred at 80 °C for 1–2 hours until a thick, dark-colored gel formed, indicating the formation of a cobalt-rich intermediate. This gel was dried and then calcined in a muffle furnace at 400 °C for 2.5 hours with a ramp rate of 5 °C min^{-1}. During calcination, the organic content decomposed, and cobalt oxide was formed, yielding porous *Alv-Co_3O_4 NSs*.

To elucidate the chemical mechanism behind the green synthesis process, the multifunctional role of *Aloe vera* in the formation of Co_3O_4 nanostructures is emphasized. *Aloe vera* acts as both a reducing and stabilizing agent due to the presence of various phytochemicals, including flavonoids, phenols, saponins, carboxylic acids, and amino acids.[9] These compounds function as electron donors and chelating agents, facilitating the reduction of cobalt ions and stabilizing the resulting nanoparticles.[9] During the synthesis, $Co(NO_3)_2 \cdot 6H_2O$ dissociates into Co^{2+} ions, which are subsequently reduced by electrons provided by the *Aloe vera* pulp, as represented below:

$$Co(NO_3)_2 \cdot 6H_2O = Co^{2+} + 2\ NO_3^{-} + 6H_2O$$

$$3Co^{2+} + 6e^{-}\ (\text{provided by } \textit{Aloe vera} \text{ pulp}) = 3Co$$

$$3Co + 2O_2 = Co_3O_4$$

These biomolecules not only drive the redox process but also act as capping agents, controlling nucleation and growth during particle formation. This results in nanostructures with tailored size, shape, and surface functionalities, which are critical for enhanced electrochemical behaviour.

2.3. Electrode preparation for electrochemical measurement

For the fabrication of the working electrode, a homogeneous slurry was prepared by mixing the as-synthesized *Alv-Co_3O_4 NSs*, conductive carbon black, and polyvinylidene fluoride (PVDF) in a weight ratio of 8 : 1 : 1 using *N*-methyl-2-pyrrolidone (NMP) as the dispersing solvent. The resulting paste was thoroughly ground and uniformly applied onto a pre-cleaned nickel foam substrate (1 × 1 cm^2). The coated electrode was subjected to vacuum drying at 80 °C overnight to eliminate residual solvent. Upon cooling to ambient temperature, the electrode was directly employed for electrochemical measurements. Prior to coating, the nickel foam was cleaned through ultrasonic treatment in deionized water and ethanol, followed by immersion in 2 M HCl for 40 minutes to remove any surface oxide layers. It was subsequently rinsed with deionized water and dried at 50 °C for 1 hour. The electrochemical tests were carried out in 1 M KOH aqueous electrolyte using the prepared electrode as the working electrode, a 2 × 2 cm^2 platinum mesh as the counter electrode, and a Saturated Calomel Electrode (SCE) as the reference electrode. A schematic representation of the synthesis process of the *Alv-Co_3O_4 NSs* and electrode fabrication is shown in Fig. 1.

3. Result and discussion

3.1. X-ray diffraction (XRD)

To investigate the crystal structure of *Alv-Co_3O_4 NSs*, synchrotron-based X-ray diffraction (XRD) measurements were performed. The high-resolution diffraction pattern, presented in Fig. 2(a), exhibits well-defined and intense peaks at 2θ values of 8.91°, 14.58°, 17.11°, 17.88°, 20.68°, 25.39°, 26.96°, 29.40°, 30.78°, 32.96°, 34.21°, 34.62°, 36.21°, 37.36°, 39.22°, and 40.30°, corresponding to the (111), (220), (311), (222), (400), (422), (511), (440), (531), (620), (533), (622), (444), (711), (642), and (731) planes, respectively. These reflections are in excellent agreement with the standard face-centered cubic (FCC) phase of Co_3O_4, assigned to the $Fd\bar{3}m$ space group (no. 227), and match well with the JCPDS card no. 42-1467.[37] The refined lattice parameter was determined to be $a = b = c = 8.08$ Å, with interaxial angles $\alpha = \beta = \gamma = 90°$, confirming the cubic symmetry of the spinel structure. The enhanced resolution of the synchrotron source allowed for precise identification of even minor reflections, highlighting the phase purity and high crystallinity of the synthesized material. The (311) reflection appears as the most intense peak, which is characteristic of spinel-type Co_3O_4.[38] The average crystallite size was found to be

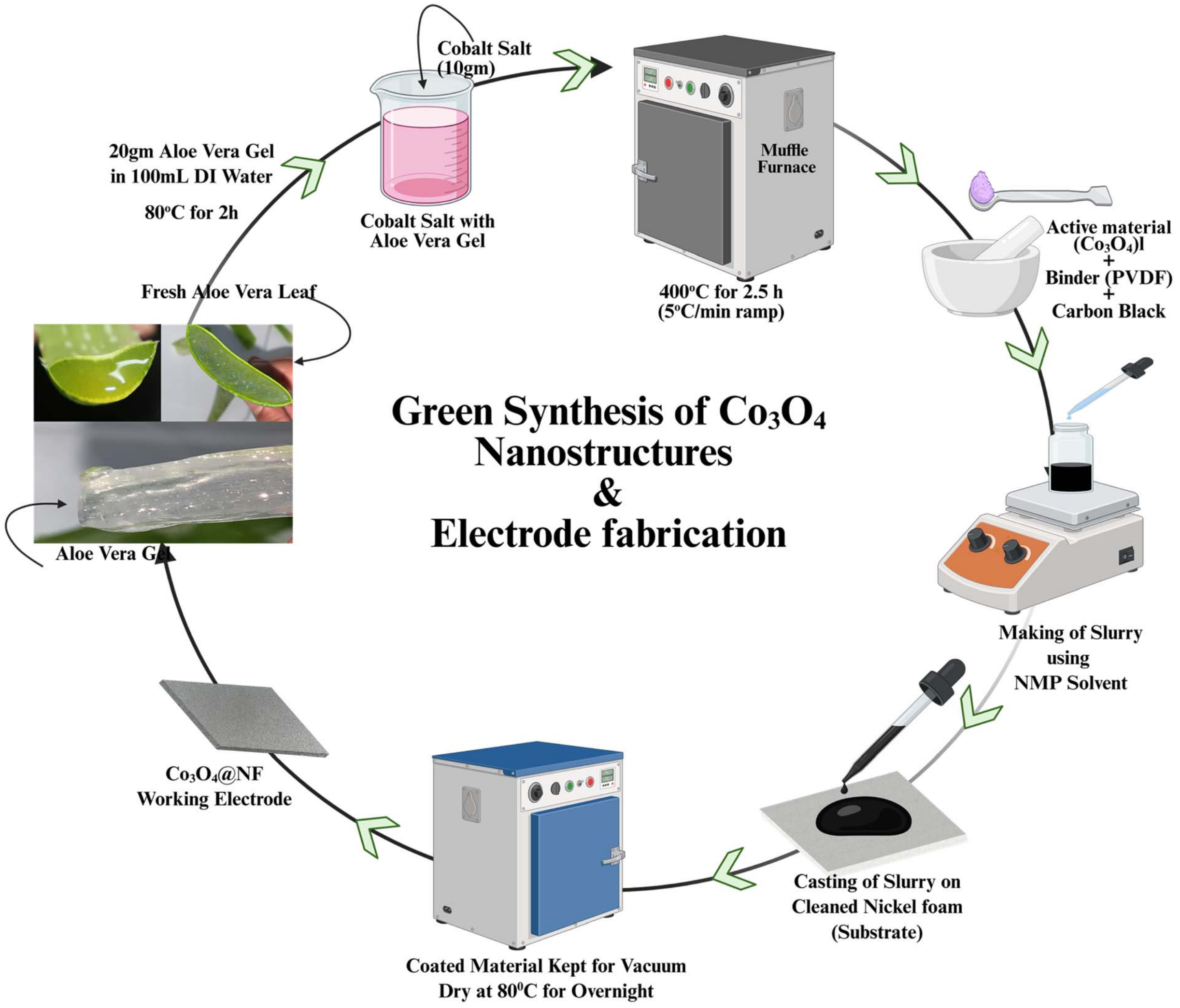

Fig. 1 Schematic illustration of the synthesis of *Alv-Co_3O_4 NSs* and fabrication of the electrode (created with Biorender.com).

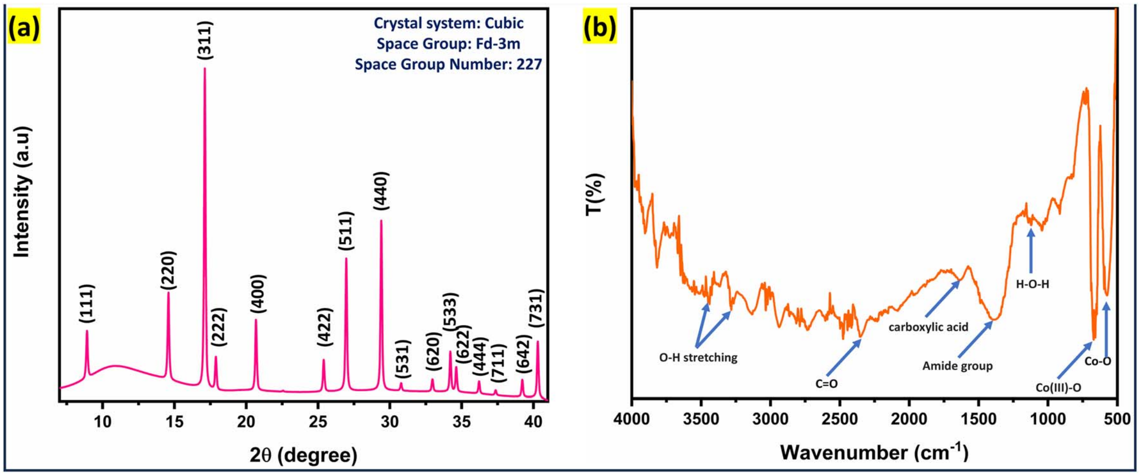

Fig. 2 (a) Synchrotron XRD pattern of *Alv-Co_3O_4 NSs* recorded in transmission mode at a wavelength of 0.072561 nm, (b) FTIR spectrum of *Alv-Co_3O_4 NSs* nanostructures recorded in the 400–4000 cm^{-1} range, confirming the formation and surface characteristics of the synthesized material.

approximately 32 nm estimated using the Scherrer equation, mentioned as following eqn (1).[39]

$$D = \frac{0.94\lambda}{\beta \cos \theta} \tag{1}$$

where D is the crystallite size, K is the shape factor (typically 0.9), λ is the X-ray wavelength (0.072561 nm), β is the full width at half maximum (FWHM) of the peak in radians, and θ is the Bragg angle.

The *Aloe vera* extract likely acted as a biotemplate and reducing agent during synthesis, contributing to the formation of well-ordered, phase-pure nanostructures.[4] The absence of impurity peaks in high quality synchrotron XRD data further affirms the effectiveness of this green synthesis route in yielding high-quality *Alv-*Co_3O_4 *NSs* with a defined crystallographic orientation.

3.2. Fourier transform infrared spectroscopy (FTIR)

FTIR is used for metal oxides to identify functional groups and confirm metal–oxygen bond formation. The functional groups present on the surface of *Alv-*Co_3O_4 *NSs* were analyzed using FTIR spectroscopy, as illustrated in Fig. 2(b). The spectrum shows distinct absorption bands that confirm the presence of both metal–oxygen bonds and plant-derived surface functionalities.[6,40] A relatively sharp band at 3430 cm^{-1} and a shoulder around 3278 cm^{-1} can be ascribed to O–H stretching vibrations, indicative of adsorbed moisture or hydroxyl groups associated with plant biomolecules.[6] The absorption band at 2350 cm^{-1} is attributed to the asymmetric stretching vibration of C═O groups, likely due to carbon dioxide interactions or plant-derived carbonyl functionalities.[6] The strong peak at 1630 cm^{-1} is characteristic of C═O bending in carboxylic acid groups, while the band at 1384 cm^{-1} corresponds to the amide group vibrations, both suggesting the presence of *Aloe vera* phytochemicals such as polyphenols and proteins.[6] A smaller band around 1121 cm^{-1} can be attributed to H–O–H bending, indicating the presence of physically adsorbed water.[40] Importantly, two intense peaks observed at 665.18 cm^{-1} and 575 cm^{-1} are characteristic of Co(III)–O and Co(II)–O stretching vibrations, respectively, which confirm the formation of spinel-phase Co_3O_4.[6] These metal–oxygen stretching modes validate the crystalline integrity and phase purity of the synthesized cobalt oxide nanostructures. The FTIR data further supports the role of *Aloe vera* extract as a bio-reducing and stabilizing agent, facilitating the green synthesis of nanostructured Co_3O_4.

3.3. Thermogravimetric analysis (TGA)

The thermal behaviour and stability of the *Alv-*Co_3O_4 *NSs* was investigated using TGA, as shown in Fig. 3(a). The sample exhibited remarkable thermal stability, with only ~3.5% weight loss observed up to 750 °C. This minimal degradation indicates the efficient removal of residual plant-derived organic components and confirms the thermal robustness of the synthesized material.[41,42] Such high stability is highly desirable for electrode materials in energy storage devices, as they are often subjected to elevated temperatures during charge and discharge cycles. The TGA results complement the FTIR analysis by confirming the minimal presence of organic matter, while also reinforcing the findings from XRD, which revealed a highly crystalline and phase-pure Co_3O_4 structure. The observed high thermal stability of the *Alv-*Co_3O_4 *NSs* provides a strong foundation for long-term electrochemical performance, as further demonstrated in the charge–discharge cycling studies.

3.4. UV-Vis spectroscopy

As shown in Fig. 3(b) UV-Vis absorption spectroscopy was employed to investigate the optical properties of the *Alv-*Co_3O_4 *NSs*, enabling the estimation of the direct band gap energy. As shown in Fig. 3(b), the Tauc plot yielded a band gap of 3.65 ± 0.10 eV (using eqn (2)), which lies at the higher end of the typical *Alv-*Co_3O_4 band gap range and aligns well with literature reports such as those by Vennela *et al.*[43] This relatively wide band gap is attributed to the quantum confinement effect,[43] particularly at the synthesized particle size of ~32 nm, and is further

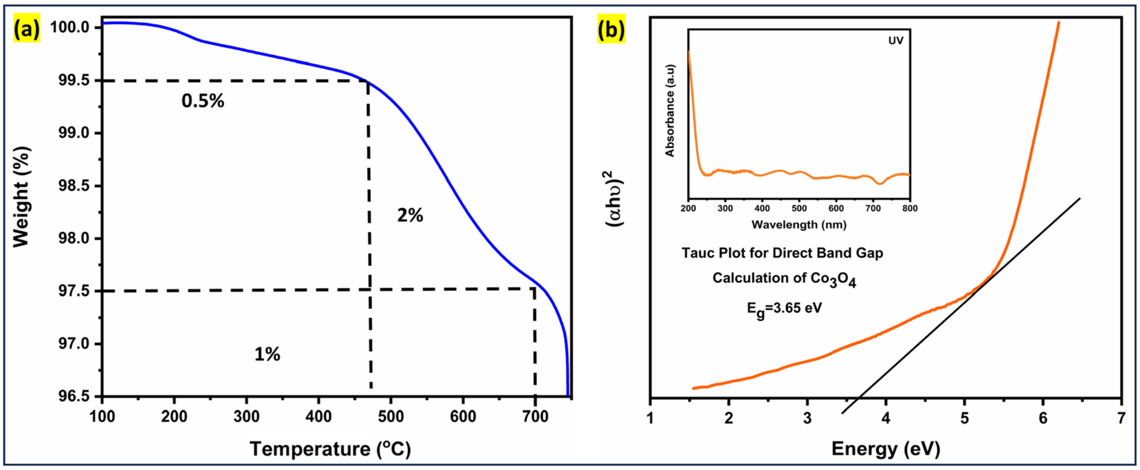

Fig. 3 (a) TGA curve of *Alv-*Co_3O_4 *NSs* showing ~3.5% weight loss up to 750 °C, indicating high thermal stability, (b) Tauc plot of *Alv-*Co_3O_4 *NSs* indicating a direct optical band gap of 3.65 ± 0.10 eV.

supported by the high crystallinity achieved through green synthesis using *Aloe vera* extract. From an energy storage perspective, such a band gap plays a critical role, it affects electronic transitions, charge transport behaviour, and the efficiency of redox reactions occurring at the electrode–electrolyte interface.[44–46] A suitable band gap ensures controlled electronic conductivity,[47] which is vital for balancing energy and power densities in supercapacitors and batteries. Moreover, the sharp absorption edge and minimal defect-related absorption suggest a low defect density,[48] contributing to excellent structural stability under electrochemical cycling. Thus, the optical features not only validate the nanoscale quality of material but also correlate strongly with its potential as a high-performance electrode material, discussed in more detail in the subsequent sections. The direct band gap (E_g) of the synthesized *Alv-*Co_3O_4 *NSs* sample was determined using Tauc's equation (eqn (2)) mentioned as following:[49]

$$(\alpha h\nu)^2 = A(h\nu - E_g) \tag{2}$$

where A is constant, α represents the optical absorption coefficient, and $h\nu$ is the photon energy.

3.5. Electron microscopy (FE-SEM/TEM)

As shown in Fig. 4 the surface morphology and microstructural characteristics of the *Alv-*Co_3O_4 *NSs* were examined through Field Emission Scanning Electron Microscopy (FE-SEM) and Transmission Electron Microscopy (TEM). Fig. 4(a) and (b) displays FESEM images at two different magnifications, revealing well-dispersed nanoparticles with uniform distribution and minimal agglomeration, suggesting effective stabilization by *Aloe vera* extract during synthesis. The Energy Dispersive X-ray Spectroscopy (EDX) spectrum shown in Fig. 4(c) confirms the elemental composition with cobalt and oxygen atomic percentages of 64.2% and 35.8%, respectively, indicating high purity of the synthesized material. TEM images in Fig. 4(d)–(f) at varying magnifications provide further evidence of uniform particle morphology, with an average particle size of approximately 35 nm, which correlates well with the crystallite size estimated from XRD analysis. These morphological insights form a crucial basis for understanding the structural advantages of the material in energy storage devices, which will be further discussed in the subsequent section on electrochemical properties.

These collective results provide a strong structural and functional basis for the excellent electrochemical behaviour observed in *Aloe vera*-assisted Co_3O_4 nanostructures. The high crystallinity and phase purity confirmed by synchrotron XRD ensure structural stability and consistent ion/electron transport during charge–discharge cycles. FTIR results confirm the presence of Co–O bonds and *Aloe vera*-derived functional groups, which not only stabilize the surface but also enhance redox activity.[9] The exceptional thermal stability observed in TGA supports long-term cycling durability by eliminating unstable organics.[9] The direct band gap (3.65 ± 0.10 eV) with a sharp absorption edge (UV-Vis) indicates low defect density and efficient charge transport, both of which are critical for fast faradaic processes.[50,51] Moreover, the uniform nanoscale morphology (∼35 nm) observed in SEM/TEM enables a high surface area, short ion diffusion pathways, and better electrode–electrolyte contact. These combined features directly contribute to the high specific capacitance, excellent rate performance, and stable cycling behaviour demonstrated in the electrochemical studies.

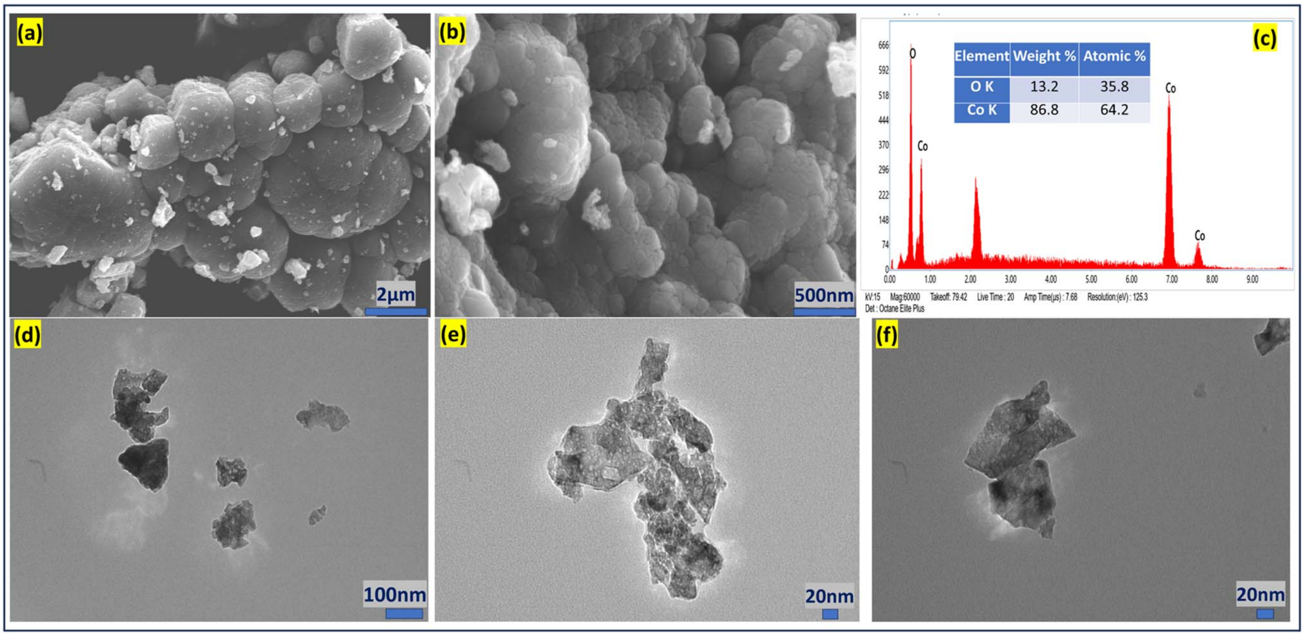

Element	Weight %	Atomic %
O K	13.2	35.8
Co K	86.8	64.2

Fig. 4 (a and b) FESEM images of *Alv-*Co_3O_4 *NSs* at two different magnifications; (c) EDX spectrum confirming elemental composition; (d–f) TEM images at varying magnifications illustrating particle dimensions and uniform nanoscale morphology.

3.6. X-ray absorption spectroscopy (XAS)

Using synchrotron XAS, we probe the local electronic structure and oxidation state of metal ions in oxides with high energy resolution. XAS reveals crystal-field splitting, ligand–metal hybridization, and unoccupied density of states, providing insights into charge-transfer mechanisms and electronic behaviour. This understanding is crucial for optimizing metal oxide materials for energy storage applications.[52]

3.6.1 Co $L_{3,2}$ edge XAS. Co $L_{3,2}$ edge XAS represents Co-2p to Co-3d dipole allowed transition and has been used as an important technique to study Co-3d unoccupied density of state. A proper analysis of $L_{3,2}$ edge XAS data provides information on oxidation states, covalency, charge transfer ground state, and spin state of the transition metal. Co_3O_4 is a direct spinel and the unit cell consists of two Co^{3+} ions in octahedral environment and one Co^{2+} ion in tetrahedral environment.

Fig. 5 shows the Co $L_{3,2}$ edge XAS spectrum. The spectrum contains two major absorption bands, marked L_3 (transition Co-L_3 → Co-3d) at around 782.2 ± 0.8 eV and L_3 (transition Co L_2 → Co-3d) around 791.1 ± 0.1 eV. A spin–orbit splitting of 14.9 ± 0.2 eV of Co 2p orbital is in agreement with literature.[52,53] The absorption bands show complex behaviour and L_3 is fit with three Gaussian peaks after subtraction of the background; as shown in the inset of Fig. 5. We observe three peaks centered at 779.3 ± 0.1 eV, 781.2 ± 0.1 eV and 782.2 ± 0.1 eV. Here the first two peaks are due to Co^{2+} and Co^{3+} transitions respectively.[53,54] The 3d orbital is split into t_{2g} and e_g sub-orbitals due to the crystal field of cations. It has also been reported that e_g is above t_{2g} in octahedral environment and opposite is true for tetrahedral environment.[55–57]

As discussed earlier, in Co_3O_4, Co^{2+} is in tetrahedral environment and hence t_{2g} will be above e_g for Co^{2+} and opposite will be true for Co^{3+}, *i.e.* $e_g < t_{2g}$. So, 779.3 and 781.2 eV transitions can be shown as below, Fig. 6.

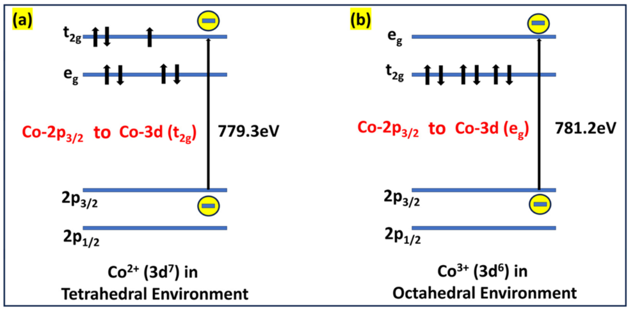

Fig. 6 Electronic transition diagram illustrating the d-orbital splitting of cobalt ions in octahedral and tetrahedral crystal fields. The diagram explains the transition mechanisms observed in *Alv-Co_3O_4 NSs* highlighting the energy levels involved in Co^{2+} (Td) and Co^{3+} (Oh) electronic transitions.

The third peak at 782.2 eV is broad and is attributed to charge transfer states. When an electron is transferred from 2p to 3d, the configuration changes from $2p^6$ ($3d^5$) ground state to $2p^5$ L ($3d^6$) ground state, where L is the hole in 2p band.

The electrochemical performance including the specific capacitance and the rate/cyclic abilities gets improved by the presence of bulk defects like anion or cation vacancies/interstitials. These defects not only present functional sites for redox improved redox reactions, but also improves the electrical conductivity of metal oxide systems.[9,53] Co $L_{3,2}$ edge XAS spectrum for Co_3O_4 sample shows peaks due to Co^{2+} in tetrahedral environment at 779.3 eV and due to Co^{3+} in octahedral environment at 781.2 eV, a difference of 1.9 eV between the two. In literature this difference is 1.65 ± 0.05 eV for Co_3O_4 and other materials, in which Co^{3+} is in octahedral environment and Co^{2+} is in tetrahedral environment.[58,59] A blue shift compared the Co^{3+} peak, is indicative of higher oxidation state

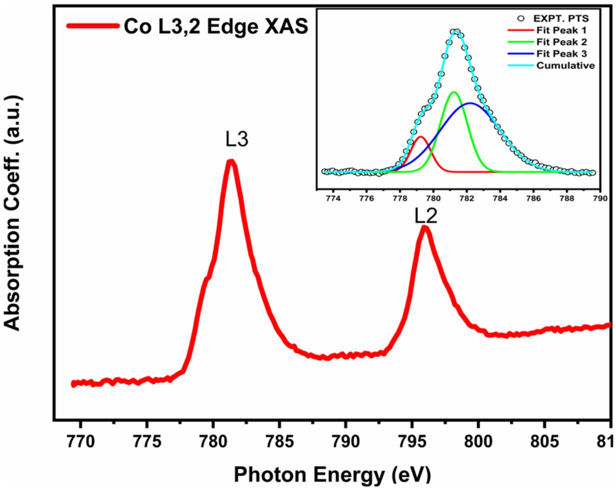

Fig. 5 Co $L_{3,2}$ edge X-ray absorption spectra of the *Alv-Co_3O_4 NSs*, acquired in total electron yield (TEY) mode. The inset displays the L_3 -edge region fitted with two Gaussian peaks after background subtraction, illustrating the distinct electronic states of Co and providing insight into its local coordination environment.

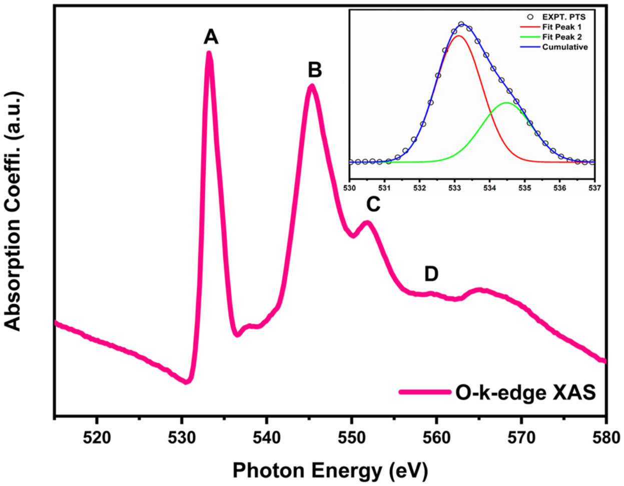

Fig. 7 Oxygen K-edge X-ray absorption spectra of *Alv-Co_3O_4 NSs*, recorded in total electron yield (TEY) mode. Features labeled as peaks 'A' and 'B' correspond to transitions associated with the transition metal L_3 and L_2 edges, respectively. These appear in the O K-edge spectrum due to strong hybridization between O 2p orbitals and transition metal 3d states.

(4+) of some Co ions in octahedral sites, resulting in bulk defects in the form of metal vacancies and/or oxygen interstitial. These bulk defects coupled with surface defects in the form of oxygen vacancies and other organic functional groups as obtained by FTIR, XPS measurements help in the improvement of electrochemical performance.

3.6.2 Oxygen K-edge XAS. Oxygen K-edge XAS for Co_3O_4 sample is shown in Fig. 7. The spectrum shows O 1s to O 2p transition and represents the intensity of transition represent covalent bandgap between Co and O. In the crystal structure of Co_3O_4, Co remains in the environment of oxygen octahedral (Co^{3+}) and tetrahedron (Co^{2+}), thus induces strong hybridisation between oxygen O and Co 3d/4s orbitals, which are depictured in Fig. 6. The absorption band mark 'A' and 'B' in Fig. 7 represent transition from O-1s to O-2p/Co-4s hybridised band and O-1s to O-2p/Co-4s hybridised bands, respectively. A different of ~12.1 eV represent between Co-3d and Co-4s orbital is in agreement with literature for $CuCoO_2$ delafossite,[53] $MnCo_2O_4$ spinel[60] and, other TM oxides.[54,61] The feature marked 'A' is further expanded and replotted in inset of Fig. 7, after subtraction of the background. The feature representing O-1s ↠ O-2p/Co-3d hybridised orbital, transition is fitted with two Gaussian, centered at 533.1 ± 0.1 eV and 534.4 ± 0.1 eV. This splitting of 1.3 ± 0.2 eV is due to crystal field splitting of Co-3d orbital into t_{2g} and e_g orbitals. The amount of crystal field splitting in our sample is in agreement with CFS of TM 3d orbital in late TM oxides and delafossite.[53]

The feature marked 'C' and 'D' in Fig. 7 at a spectrum of ~6.6 eV ('C') and ~14.4 eV ('D'), from the feature "B", are EXAFS-LIKE effect due to interference between the photoelectron wave generated from any arbitrarily chosen oxygen atom and the reflected wave from the neighbouring atoms.[62] The authors suggested an empirical relation $\varepsilon_r R_2 = \text{constant}$, connecting the separation between the features 'B' and 'C' (ε_r) and distance between the oxygen atoms (R), using the relation. We find the distance between the oxygen atoms to be 3.1 Å.

The XAS analysis revealed distinct Co^{2+} and Co^{3+} states with pronounced crystal field splitting and strong Co–O hybridization, indicating a well-defined electronic structure essential for redox activity. These electronic features are further supported by synchrotron XRD, which confirms the formation of highly crystalline, phase-pure spinel Co_3O_4, and by FTIR spectra showing characteristic Co–O stretching along with *Aloe vera*-derived organic residues that act as surface functional groups.

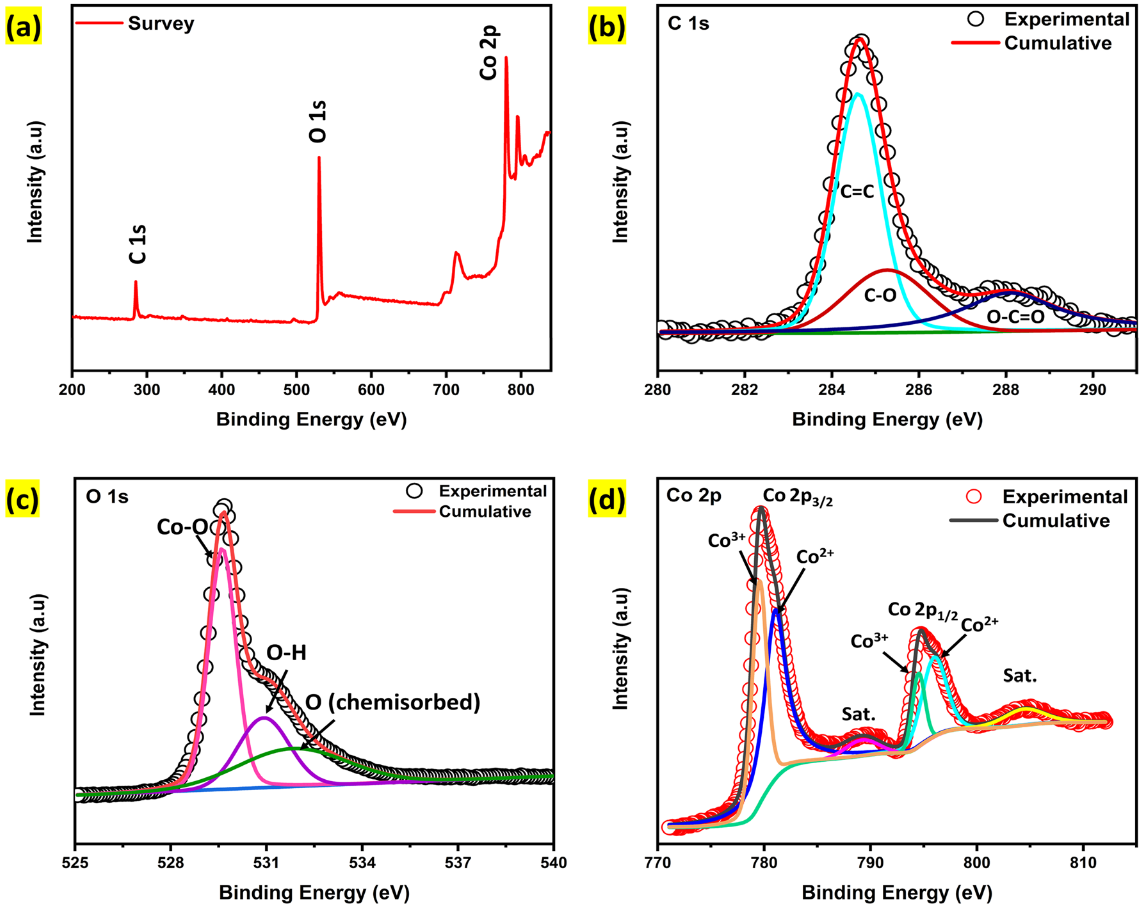

Fig. 8 X-ray photoelectron spectroscopy (XPS) analysis of *Alv-Co$_3$O$_4$ NSs*: (a) survey spectrum showing the presence of cobalt, oxygen, and surface carbon; (b) C 1s spectrum indicating surface organic functional groups derived from *Aloe vera* extract; (c) O 1s spectrum revealing lattice oxygen, surface hydroxyls, and chemisorbed oxygen species; (d) high-resolution Co 2p spectrum confirming the coexistence of Co^{2+} and Co^{3+} oxidation states along with satellite features, consistent with the spinel structure.

UV-Vis spectroscopy revealed a direct band gap of 3.65 ± 0.10 eV, indicating low defect density and enhanced charge transport properties. Notably, the green synthesis route using *Aloe vera* not only replaces hazardous chemicals with bioactive phytochemicals but also promotes controlled nucleation, surface passivation, and crystallinity. This eco-friendly approach results in a structurally ordered and electronically favourable Co_3O_4 nanostructure, optimizing it for energy storage applications. The improved electrochemical behaviour of the *Alv-Co_3O_4 NSs* is experimentally validated in following Section 3.7.

3.7. X-ay photoelectron spectroscopy (XPS)

To elucidate the surface functional groups and to reconfirm the oxidation states (obtained using XAS as discussed in Section 3.6) of the *Alv-Co_3O_4 NSs*, XPS measurement was conducted. The survey spectrum (Fig. 8(a)) confirms the presence of Co, O, and adventitious C. The C 1 s spectrum (Fig. 8(b)) shows three distinct peaks at 284.6 eV, 286.1 ± 0.2 eV, and 288.3 ± 0.2 eV, corresponding to adventious C=C, C–O, and O–C=O groups, respectively. The adventious C=C obtained at 284.6 eV, shows no major charging effect and hence no shift in B.E. was applied for interpretation of the XPS data. The signals for –O–C=O group is attributed to residual *Aloe vera* phytochemicals adsorbed on the material surface during green synthesis, which contribute to surface passivation and defect minimization.[63] The O 1s core-level spectrum (Fig. 8(c)) is fit with three Gaussian peaks. The main peak at 529.5 ± 0.2 eV is attributed to lattice oxygen (Co–O bonds), while the second peak at 530.7 ± 0.2 eV is associated with surface oxygen atoms partially substituted by hydroxyl groups (–OH). The third component at 531.3 ± 0.2 eV corresponds to chemisorbed oxygen species, indicative of low-coordination surface sites or oxygen vacancies.[64] These oxygen species play a critical role in enhancing redox activity and electron transport, in agreement with the strong Co–O hybridization and oxygen ligand-field splitting observed in the O K-edge XAS analysis.[65]

The high-resolution Co 2p spectrum (Fig. 8(d)) confirms the presence of mixed-valent cobalt. The spectrum was deconvoluted into six components, including two main peaks at 779.5 ± 0.2 eV (Co $2p_{3/2}$) and 795.9 ± 0.2 eV (Co $2p_{1/2}$), along with their corresponding satellite peaks. The observed spin–orbit splitting of ~15 eV is consistent with the values reported in literature. Main $2p_{3/2}$ and $2p_{1/2}$ peaks are further deconvoluted using Gaussian peaks and the two peaks are located at 781.1 ± 0.2 and 779.5 ± 0.2 eV, corresponding to Co^{2+} and Co^{3+}, respectively. The presence of both Co^{2+} and Co^{3+} oxidation states, as also

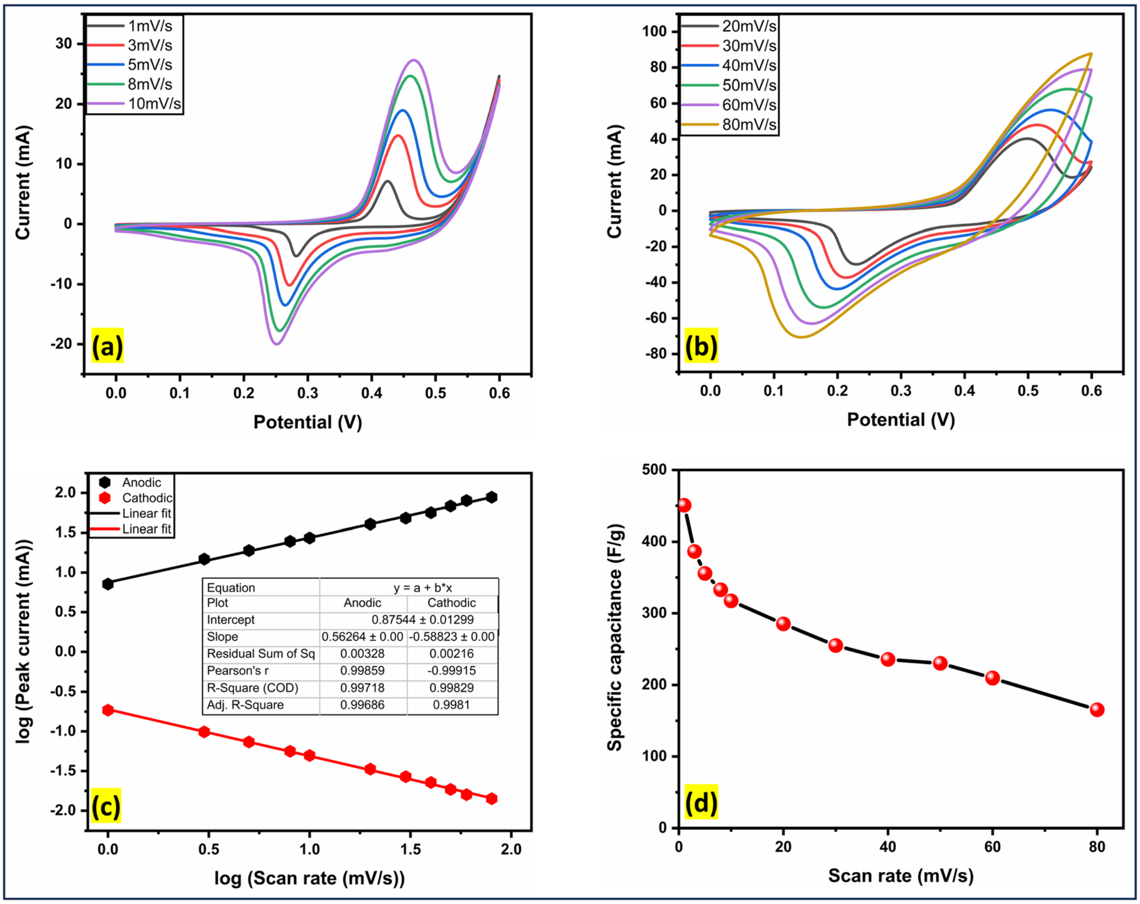

Equation	y = a + b*x	
Plot	Anodic	Cathodic
Intercept	0.87544 ± 0.01299	
Slope	0.56264 ± 0.00	-0.58823 ± 0.00
Residual Sum of Sq	0.00328	0.00216
Pearson's r	0.99859	-0.99915
R-Square (COD)	0.99718	0.99829
Adj. R-Square	0.99686	0.9981

Fig. 9 (a and b) Cyclic voltammetry (CV) curves of *Alv-Co_3O_4 NSs* electrode at various scan rates ranging from 1 to 80 mV s^{-1}, (c) anodic and cathodic peak current plot *versus* scan rate, (d) specific capacitance trend with increasing scan rate.

evidenced in the Co $L_{3,2}$-edge XAS results. These findings support the structural model of Co_3O_4 as a direct spinel oxide comprising Co^{2+} ions in tetrahedral and the two Co^{3+} ions in two octahedral environments, crucial for multivalent redox activity.[64]

These spectroscopic insights, particularly the coexistence of Co^{2+}/Co^{3+} oxidation states, strong Co–O hybridization, and well-resolved crystal field splitting, translate directly into enhanced redox activity and improved charge transport at the electrode–electrolyte interface. The charge transfer feature observed at 782.2 eV indicates strong metal–ligand covalency, which supports rapid electron hopping and boosts redox kinetics. Additionally, the low defect density inferred from the sharp absorption features and the EXAFS-like oscillations confirm a well-ordered local environment, contributing to structural stability during prolonged cycling. Such features are essential for facilitating fast and reversible faradaic reactions, which underpin the high specific capacitance (467.9 F g^{-1} at 0.5 A g^{-1}) and excellent cycling stability observed in the following electrochemical evaluations (Section 3.8). Thus, the combined XPS and XAS results offer a direct structure–function correlation that explains the superior electrochemical performance of *Alv-*Co_3O_4 *NSs*.

Taken together, the structural, spectroscopic, and morphological analyses, provide a strong structural and functional basis for the excellent electrochemical behaviour observed in *Alv-*Co_3O_4 *NSs*. The high crystallinity and phase purity confirmed by synchrotron XRD ensure structural stability and consistent ion/electron transport during charge–discharge cycles. FTIR results confirm the presence of Co–O bonds and *Aloe vera*-derived functional groups, which not only stabilize the surface but also enhance redox activity.[9] Furthermore, the electrochemical performance, including the specific capacitance and rate/cyclic abilities, is significantly enhanced by the presence of bulk defects such as anion or cation vacancies and interstitials. These defects act as active redox sites and facilitate improved electronic conductivity in metal oxide systems.[9,53] The Co $L_{3,2}$ edge XAS spectrum of the Co_3O_4 sample reveals Co^{2+} in tetrahedral coordination (779.3 eV) and Co^{3+} in octahedral coordination (781.2 eV), a separation of 1.9 eV, slightly higher

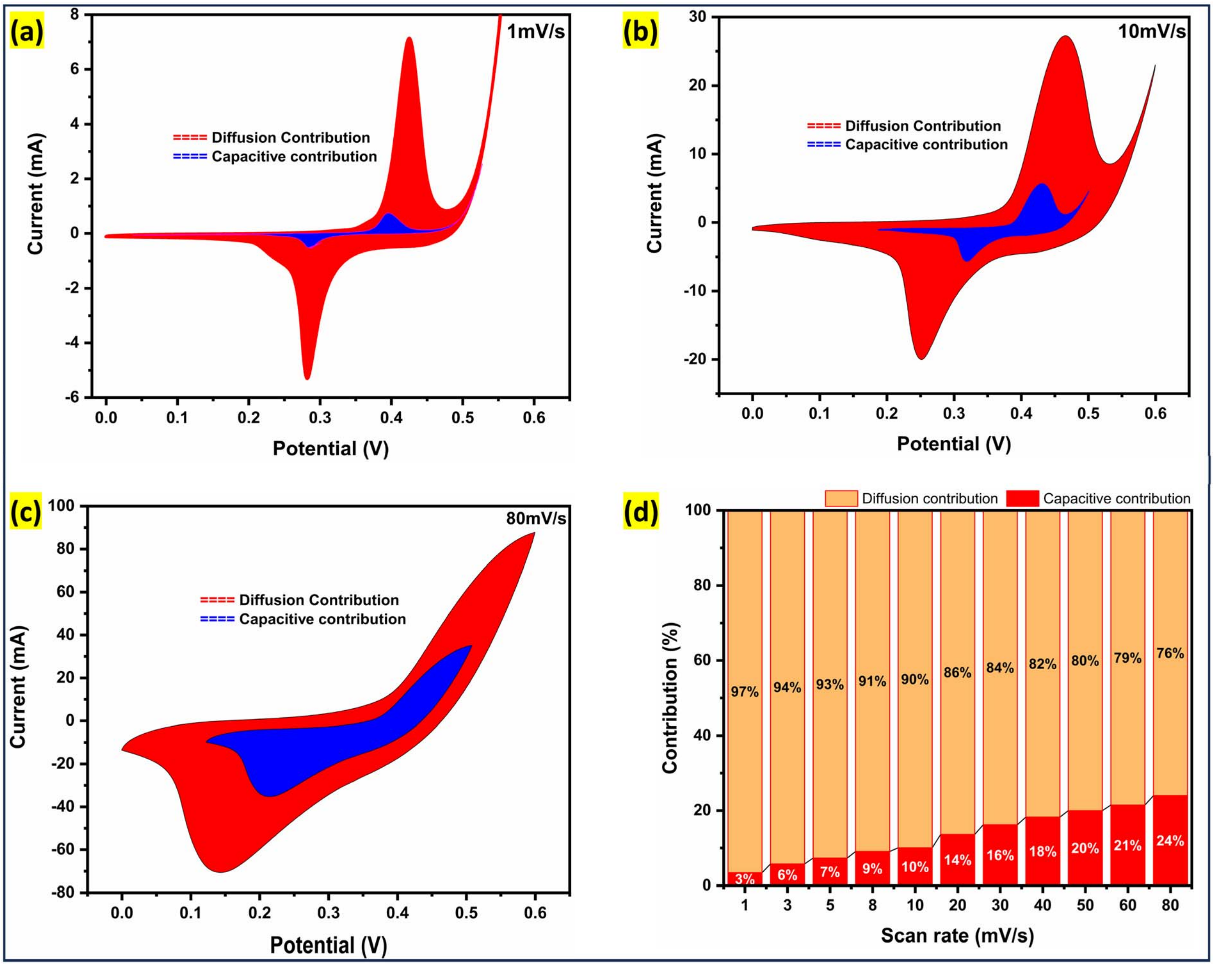

Fig. 10 (a) Separation of capacitive and diffusion-controlled contributions at a low scan rate, indicating predominant diffusion (battery-type) behavior. (b and c) Charge storage contribution analysis at scan rates of 10 and 80 mV s^{-1}, respectively, showing increasing surface-controlled (capacitive) behaviour with scan rate. (d) Plot of capacitive and diffusion-controlled contributions as a function of scan rate, highlighting the transition toward surface-dominated charge storage at higher scan rates.

than the 1.65 ± 0.05 eV typically reported for Co_3O_4 and related materials.[58,59] This blue shift suggests the presence of Co^{4+} in octahedral sites, implying the formation of metal vacancies and/or oxygen interstitials. These bulk defects, along with surface defects such as oxygen vacancies and *Aloe vera*-derived organic functional groups (as supported by FTIR and XPS), synergistically enhance the electrochemical activity. The exceptional thermal stability observed in TGA further supports long-term cycling durability by eliminating unstable organics. The direct band gap (3.65 ± 0.10 eV) with a sharp absorption edge (UV-Vis) indicates low intrinsic defect density and efficient charge transport, both critical for fast faradaic processes.[50,51] Moreover, the uniform nanoscale morphology (∼35 nm) observed in SEM/TEM enables a high surface area, short ion diffusion pathways, and superior electrode–electrolyte contact. Together, these structural and chemical features result in the observed high specific capacitance, excellent rate performance, and stable cycling behavior.

3.8. Electrochemical measurements (EC)

EC serve as a pivotal approach to understand the charge storage behaviour and redox activity of electrode materials in supercapacitor applications. In this study, the electrochemical performance of the synthesized *Alv-Co$_3$O$_4$ NSs* nanostructure was assessed using cyclic voltammetry (CV), galvanostatic charge–discharge (GCD), long-term cycling stability, and electrochemical impedance spectroscopy (EIS). All measurements were performed in a three-electrode configuration using 1 M KOH aqueous solution as the electrolyte. CV was conducted over a range of scan rates from 1 to 80 mV s^{-1}, GCD was performed at current densities ranging from 0.5 A g^{-1} to 10 A g^{-1}, and EIS analysis was carried out within the frequency range of 10 mHz to 100 kHz.

3.8.1 Cyclic voltammetry (CV). The electrochemical behaviour of *Alv-Co$_3$O$_4$ NSs* was investigated through CV at various scan rates ranging from 1 to 80 mV s^{-1}, as shown in Fig. 9(a) and (b). All CV curves exhibit prominent redox peaks, confirming the pseudocapacitive nature arising from the reversible redox transitions of Co^{2+}/Co^{3+}.[66] At lower scan rates (Fig. 9(a)), well-defined redox peaks are clearly observed, while at higher scan rates (Fig. 9(b)), these peaks shift slightly toward higher potentials (anodic) and lower potentials (cathodic), respectively. This shift is attributed to internal resistance and kinetic limitations at faster ion diffusion rates a typical characteristic of pseudocapacitive materials.[67] The increasing peak current with scan rate and the broadening of redox peaks

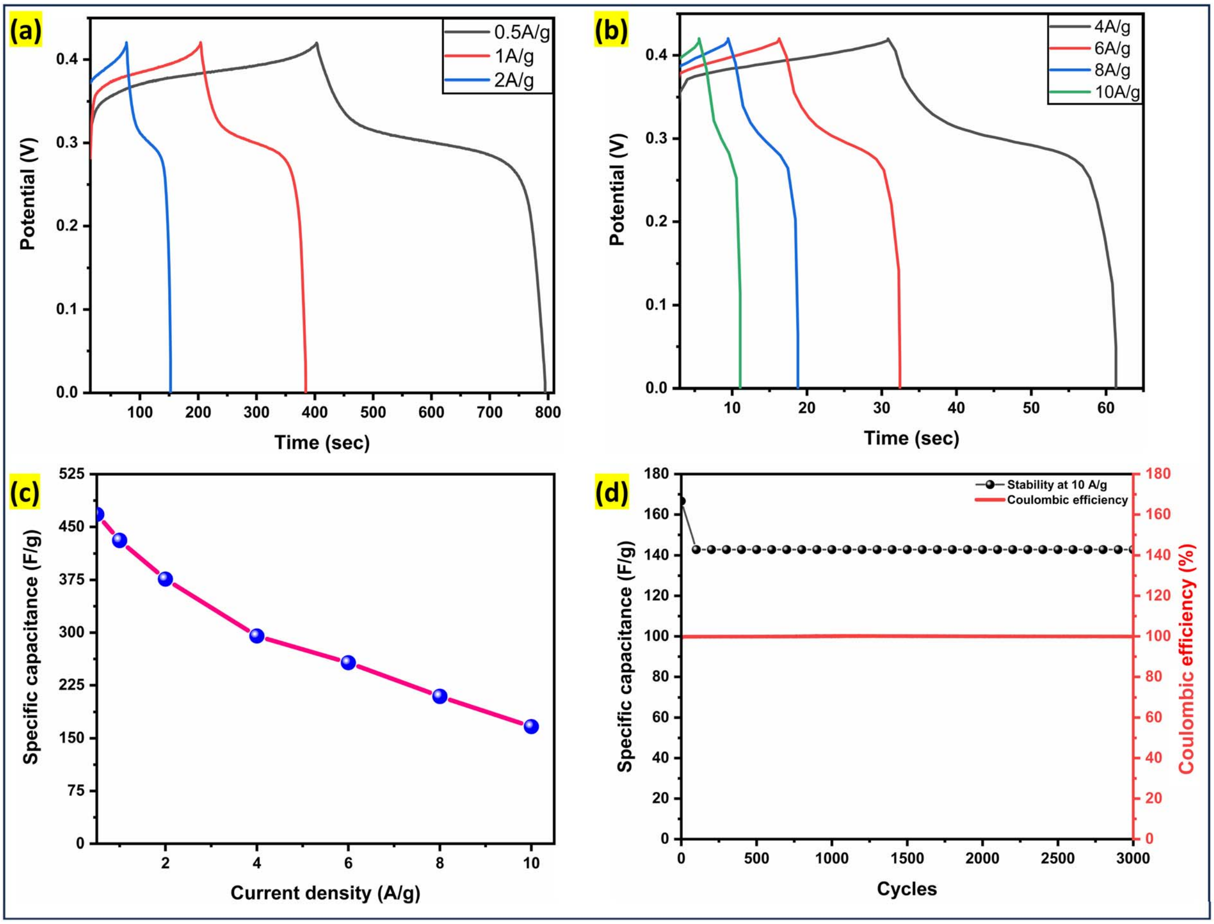

Fig. 11 (a and b) GCD profiles of *Alv-Co$_3$O$_4$ NSs* at different current densities; (c) Specific capacitance as a function of current density; (d) cycling stability and coulombic efficiency over 3000 cycles at 10 A g^{-1}.

further supports the efficient faradaic processes occurring at the electrode surface. The quasi-rectangular CV shape at low scan rates and the presence of sharp, symmetric peaks suggest a battery-type faradaic behaviour. The area under the CV curve increases progressively with scan rate, indicating enhanced charge storage capability.

To further explore the kinetics of the redox process, the relationship between peak current (i) and scan rate (v) was analysed using the power-law eqn (3), as shown in Fig. 9(c),[68] the calculated b-value of 0.57 suggests that the charge storage mechanism is primarily diffusion-controlled, typical of battery-type materials with significant faradaic contribution rather than surface-limited capacitive processes.[3]

$$i_{\mathrm{p}} = av^{b} \tag{3}$$

The calculated specific capacitance (C_{sp}, in F g^{-1}) values using eqn (4)[3,69] at different scan rates are, 450.66 F g^{-1} at 1 mV s^{-1}, 386.44 F g^{-1} at 3 mV s^{-1}, 355.74 F g^{-1} at 5 mV s^{-1}, 332.81 F g^{-1} at 8 mV s^{-1}, 317.38 F g^{-1} at 10 mV s^{-1}, 285.08 F g^{-1} at 20 mV s^{-1}, 254.75 F g^{-1} at 30 mV s^{-1}, 235.42 F g^{-1} at 40 mV s^{-1}, 229.97 F g^{-1} at 50 mV s^{-1}, 209.58 F g^{-1} at 60 mV s^{-1}, and 165.46 F g^{-1} at 80 mV s^{-1}, as shown in Fig. 9(d). These results collectively demonstrate that the *Alv-Co_3O_4 NSs* exhibits a typical battery-type pseudocapacitive behaviour with high specific capacitance and efficient diffusion-controlled kinetics, making it a strong candidate for high-performance supercapattary electrode materials.

$$C_{\mathrm{sp}} = \frac{A}{2mk\Delta V} \tag{4}$$

where, A is the integrated area under the CV curve, m is the mass of active material in grams, k is the scan rate in V s^{-1}, and ΔV is the potential window in volts.

To further elucidate the underlying charge storage mechanism, the capacitive and diffusion-controlled contributions were quantitatively analyzed based on CV data, as depicted in Fig. 10. Using Dunn method, the total current response at a given potential ($i(V)$) can be expressed as a combination of capacitive (surface-controlled) and diffusion-controlled (bulk faradaic) processes, following the eqn (5),[70]

$$i(V) = k_1 v + k_2 v^{1/2} = I_{\mathrm{capacitive}} + I_{\mathrm{diffusion}} \tag{5}$$

where $k_1 v$ corresponds to the capacitive contribution and $k_2 v^{1/2}$ represents the diffusion-controlled contribution.

As shown in Fig. 10(a), at a lower scan rate, the current response is predominantly governed by diffusion-controlled

Table 1 Comparison of the electrochemical performance and synthesis approaches of *Alv-Co_3O_4 NSs* with previously reported Co_3O_4-based electrode materials

Material	Electrolyte	Synthesis	Specific capacitance	Reference
Alv-Co_3O_4 NSs	1 M KOH	Green synthesis	430.95 F g^{-1} at 1 A g^{-1} 450.66 F g^{-1} at 1 mV s^{-1}	This work
Co_3O_4 autocombustion	1 M KOH	Sol–gel method and calcination	162 F g^{-1} at 0.25 A g^{-1}	71
MWCNTs@Co_3O_4	3 M KOH	Thermal annealing	206.89 F g^{-1} at 1 A g^{-1}	72
Co_3O_4–graphene composite	1 M KOH	Co-precipitation	140 F g^{-1} at 20 mV s^{-1}	73
Co_3O_4 nanosheet	2 M KOH	Hydrothermal	356.6 F g^{-1} at 0.4 A g^{-1}	74
Co_3O_4 core shell microsphere	2 M KOH	Hydrothermal	261.1 F g^{-1} at 0.5 A g^{-1}	75
Co_3O_4 nanoplates	2 M KOH	Reflux	225 F g^{-1} at 2 A g^{-1}	76
Co_3O_4 nanorods	6 M KOH	Calcination	262 F g^{-1} at 5 mV s^{-1}	77
Co_3O_4	6 M KOH	Co-precipitation	239.5 F g^{-1} at 0.5 A g^{-1}	78
Co_3O_4/MWCNTs	6 M KOH	Chemical deposition	273 F g^{-1} at 0.5 A g^{-1}	79
Co_3O_4/graphene hybrid fibers	2 M KOH	Annealed	236.8 F g^{-1} at 0.2 A g^{-1}	80
Co_3O_4 nanostructures	1 M KOH	Facial synthesis	150.65 F g^{-1} at 1 mA cm^{-2}	81
Co_3O_4 nanoparticles	3 M KOH	Phyto-assisted co-precipitation	217.4 F g^{-1} at 2 mV s^{-1} 115.15 F g^{-1} at 0.5 A g^{-1}	82
Co_3O_4@carbon	6 M KOH	Oxygen-assisted pyrolysis	148 F g^{-1} at 1 A g^{-1}	83
Co_3O_4 nanorods	2 M KOH	Hydrothermal and calcination	318 F g^{-1} at 1 A g^{-1}	84
Co_3O_4	2 M KOH	Hydrothermal	73 F g^{-1} at 1 mA cm^{-2}	85
Co_3O_4@CoCH	2 M KOH	Hydrothermal	440 F g^{-1} (1541 mF cm^{-2}) at 1 mA cm^{-2}	85
Co_3O_4 nanosheets	2 M NaOH	Hydrothermal and calcination	610 mF cm^{-2} at 1 mA cm^{-2}	86
Co_3O_4/$Co(OH)_2$ nanoflakes	1 M KOH	Electrodeposition	601 mF cm^{-2} at 2 mA cm^{-2}	87
Co_3O_4 electrode	0.5 Na_2SOO_4	Electrodeposition	315 F g^{-1} at 5 mV s^{-1}	88
Co_3O_4 tubules	3 M KOH	Oil bath	326 F g^{-1} at 1 A g^{-1}	89
Co_3O_4 plates	2 M KOH	Hydrothermal and calcination	350.8 F g^{-1} at 1 A g^{-1}	74
Co_3O_4 nanorods	6 M KOH	Hydrothermal	146 F g^{-1} at 1 A g^{-1}	77
Co_3O_4 nanoplates	2 M KOH	Facile reflux method	225 F g^{-1} at 2 A g^{-1}	76
Co_3O_4 microsphere	3 M KOH	Room temperature interfacial-reaction	261.1 F g^{-1} at 0.5 A g^{-1}	75
Co_3O_4/graphite nanocomposite	6 M KOH	Co-precipitation and calcination	395.04 F g^{-1} at 0.5 A g^{-1}	78
Co_3O_4/CoO@carbon nanocomposite	—	Pyrolysis and hydrothermal	324 C g^{-1} at 1 A g^{-1}	90
Co_3O_4 composite	6 M KOH	Hydrothermal and calcination	411.76 F g^{-1} at 1 A g^{-1}	91

processes, indicative of a battery-type material wherein faradaic redox reactions plays a significant role in charge storage.[33,70] This aligns well with the earlier *b*-value analysis and the observation of redox peaks in the CV curves. Fig. 10(b) and (c) present the quantitative separation of surface-controlled and diffusion-controlled contributions at scan rates of 10 mV s^{-1} and 80 mV s^{-1}, respectively. A notable increase in the surface-controlled (capacitive) contribution is observed with increasing scan rate. This shift is attributed to the limited time available for ion diffusion into the bulk of the electrode material at higher scan rates, resulting in a larger proportion of the charge being stored at or near the electrode surface. The variation of capacitive and diffusion-controlled contributions with respect to scan rate is summarized in Fig. 10(d). It clearly demonstrates a progressive increase in the capacitive (surface-dominated) behaviour with increasing scan rate, highlighting the dual charge storage capability of material. At lower scan rates, diffusion processes dominate due to sufficient time for electrolyte ions to penetrate deep into the active material, while at higher scan rates, the surface-driven capacitive processes become more pronounced due to kinetic limitations.[33] These findings confirm that *Alv-*Co_3O_4 *NSs* exhibits a hybrid energy storage mechanism, transitioning from diffusion-controlled to increasingly surface-controlled behaviour as scan rate increases, an essential trait for high-rate supercapacitor applications.

3.8.2 Galvanostatic charge–discharge (GCD). GCD profiles of *Alv-*Co_3O_4 *NSs*, as shown in Fig. 11(a) and (b), exhibit nearly symmetrical charge–discharge curves across various current densities, confirming excellent electrochemical reversibility and low *IR* drop. The specific capacitance values, calculated using discharge time from the GCD curves (using eqn (6)),[68] are found to be 467.85, 430.95, 376.19, 295.23, 257.14, 209.52, and 166.67 F g^{-1} at 0.5, 1, 2, 5, 8, and 10 A g^{-1}, respectively. This trend, presented in Fig. 11(c), indicates a gradual decrease in capacitance with increasing current density, which is attributed to limited diffusion of electrolyte ions at higher rates.[3]

$$C_{\mathrm{sp}} = \frac{I_{\mathrm{m}} \times \Delta t}{\Delta V} \tag{6}$$

where, I_{m} is the current density (A g^{-1}), Δt is the discharge time (s), and ΔV is the potential window (V).

This aligns with CV analysis where diffusion-dominated charge storage prevails at low scan rates, while surface-driven pseudocapacitive contributions become more significant at higher scan rates. Furthermore, the long-term cycling performance of the *Alv-*Co_3O_4 *NSs* electrode, shown in Fig. 11(d), highlights its excellent electrochemical durability. The electrode retains 83% of its initial capacitance after 3000 continuous charge–discharge cycles at 10 A g^{-1}. Interestingly, 17% of drop occurs in the first 100 cycles, likely due to structural activation and minor rearrangements at the electrode–electrolyte interface. However, beyond this initial phase, the device exhibits remarkable structural stability, maintaining ∼100% retention from 100 to 3000 cycles. Simultaneously, the coulombic efficiency remains stable at ∼100% throughout the cycling, confirming the high reversibility and minimal degradation of material. A comparison of electrochemical performance of our green synthesised *Alv-*Co_3O_4 *NSs* material with other reported methods is provided in Table 1, further emphasizing its electrochemical performance and environmental sustainability.

3.8.3 Electrochemical impedance spectroscopy (EIS). EIS was conducted in the frequency range of 10 mHz to 100 kHz to assess the internal resistance and interface stability of *Alv-*Co_3O_4 *NSs* electrode. As depicted in Fig. 12(a) and (b), the Nyquist plots show a small intercept on the real axis in the high-frequency region, followed by a near-vertical line in the low-frequency region, indicative of dominant capacitive behaviour and efficient ion diffusion. The solution resistance (R_{s}), derived from the high-frequency *x*-axis intercept, was found to be 1.19 Ω before and 1.29 Ω after the complete electrochemical testing, including CV, GCD and stability. The minimal increase in R_{s} confirms the excellent conductivity of electrode, robust structural integrity, and stable electrode–electrolyte interface throughout the entire testing process.

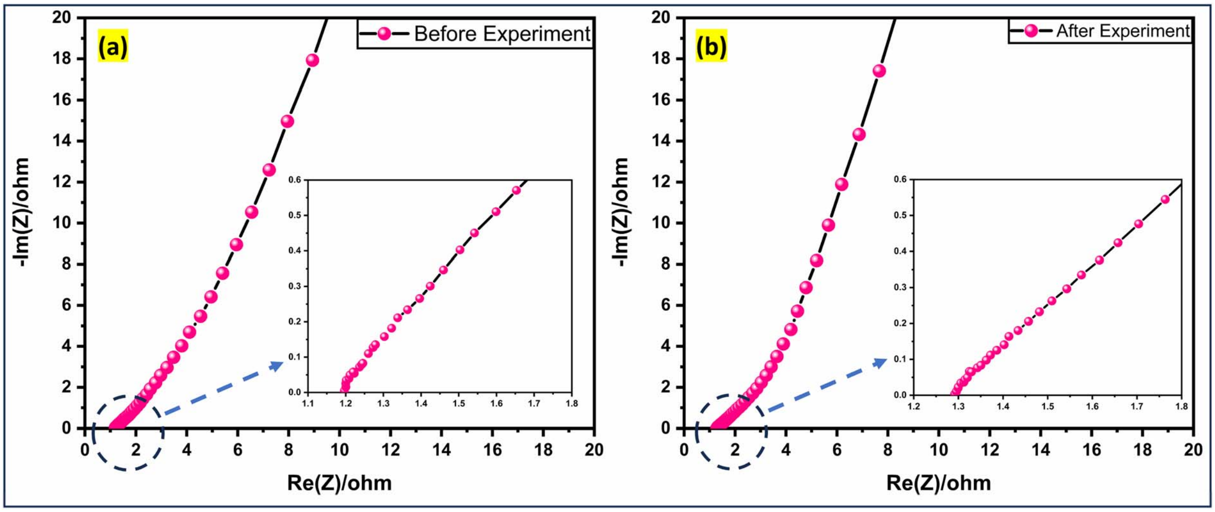

Fig. 12 Nyquist plots of *Alv-*Co_3O_4 *NSs* electrode (a) before and (b) after electrochemical measurements.

4. Conclusion

In this study, *Aloe vera*-assisted Co_3O_4 nanostructures (*Alv-Co_3O_4 NSs*) were successfully synthesized using green synthesis route. Synchrotron XRD confirmed the formation of a highly crystalline, phase-pure spinel Co_3O_4 with an average crystallite size of approximately 32 nm. SEM and TEM images showed uniform, well-dispersed nanoparticles, stabilized effectively by *Aloe vera* phytochemicals as indicated by FTIR, which also revealed characteristic Co–O bonding and organic functional groups. TGA demonstrated excellent thermal stability with minimal weight loss up to 750 °C, ensuring robustness under operational conditions. The XAS measurements provided key insights into the Co oxidation states, confirming the coexistence of Co^{2+} in tetrahedral and Co^{3+} in octahedral sites, along with clear crystal field splitting and strong Co–O hybridization. These XAS findings were further supported by X-ray photoelectron spectroscopy (XPS), which confirmed the presence of Co^{2+}/Co^{3+} oxidation states, characteristic satellite features, and chemisorbed oxygen species, highlighting surface-level redox-active sites and oxygen vacancies that facilitate enhanced charge transport. UV-Vis spectroscopy indicated a direct band gap of 3.65 ± 0.10 eV, highlighting low defect density and favourable electronic structure conducive to efficient charge transport. Electrochemical studies revealed that these structural and electronic features translate to impressive performance: a high specific capacitance of 450.66 F g^{-1} at 1 mV s^{-1} and 467.9 F g^{-1} at 0.5 A g^{-1}, excellent rate capability, and remarkable cycling stability, retaining about 83% of capacitance after 3000 cycles with near-perfect coulombic efficiency. The initial 17% capacitance loss observed within the first 100 cycles is attributed to electrode activation and interface rearrangement, after which the electrode performance stabilized, reflecting the intrinsic durability of material. Together, these results demonstrate that the *Aloe vera*-based green synthesis not only offers a sustainable and eco-friendly fabrication route but also produces Co_3O_4 nanostructures with optimized structural, electronic, and surface properties that enhance their suitability as electrode materials for hybrid supercapattery applications. This work underscores the potential of integrating green chemistry with advanced characterization to advance energy storage applications.

Author contributions

M. B.: conceptualization, investigation, data curation, formal analysis, methodology, visualization, writing – original draft. K. G.: conceptualization, methodology, formal analysis, writing – review & editing. P. D.: formal analysis. A. K. S.: supervision, project administration, writing – review & editing.

Conflicts of interest

The authors declare that they have no known competing financial interests or personal relationships that could have appeared to influence the work reported in this paper.

Data availability

The datasets generated during the current study are available from the authors upon reasonable request.

Acknowledgements

M. B. acknowledges Dr Archana Sagdeo XRD BL-12, Indus-2, RRCAT Indore and Dr Mukul Gupta XAS BL-01, Indus-2, RRCAT Indore, and R&D- UPES, Dehradun for providing the necessary research infrastructure and JRF fellowship to M. B.

References

1 Z. M. Almarhoon, T. Indumathi and E. R. Kumar, *J. Mater. Sci.: Mater. Electron.*, 2022, **33**, 23659–23672.
2 N. A. I. Md Ishak, S. K. Kamarudin and S. N. Timmiati, *Mater. Res. Express*, 2019, **6**, 112004.
3 M. Bhatt, B. Gupta and A. K. Sinha, *Sci. Rep.*, 2025, **15**, 2192.
4 M. Bulla, V. Kumar, R. Devi, S. Kumar, A. K. Sisodiya, R. Dahiya and A. K. Mishra, *Sci. Rep.*, 2024, **14**, 7389.
5 S. Iravani, *Green Chem.*, 2011, **13**, 2638.
6 P. Chelliah, S. M. Wabaidur, H. P. Sharma, M. J. Jweeg, H. Sh. Majdi, M. M. R. A. Kubaisy, A. Iqbal and W.-C. Lai, *Water*, 2023, **15**, 910.
7 K. Pal, S. Chakroborty and N. Nath, *Green Process. Synth.*, 2022, **11**, 951–964.
8 R. Saxena, S. Kotnala, S. C. Bhatt, M. Uniyal, B. S. Rawat, P. Negi and M. K. Riyal, *Sustain. Chem. Clim. Action*, 2025, **6**, 100071.
9 M. Bhatt, K. Gautam, A. Verma and A. K. Sinha, *Mater. Adv.*, 2025, DOI: 10.1039/D5MA00556F.
10 A. I. Osman, Y. Zhang, M. Farghali, A. K. Rashwan, A. S. Eltaweil, E. M. Abd El-Monaem, I. M. A. Mohamed, M. M. Badr, I. Ihara, D. W. Rooney and P.-S. Yap, *Environ. Chem. Lett.*, 2024, **22**, 841–887.
11 J. Singh, T. Dutta, K.-H. Kim, M. Rawat, P. Samddar and P. Kumar, *J. Nanobiotechnol.*, 2018, **16**, 84.
12 C. Wu, T. Zhang, B. Ji, Y. Chou and X. Du, *Cellulose*, 2024, **31**, 4849–4864.
13 A. Diallo, A. C. Beye, T. B. Doyle, E. Park and M. Maaza, *Green Chem. Lett. Rev.*, 2015, **8**, 30–36.
14 O. J. Nava, P. A. Luque, C. M. Gómez-Gutiérrez, A. R. Vilchis-Nestor, A. Castro-Beltrán, M. L. Mota-González and A. Olivas, *J. Mol. Struct.*, 2017, **1134**, 121–125.
15 N. O. Sanjeev, M. S. Vallabha and A. E. Valsan, *Environ. Res.*, 2024, **252**, 119047.
16 S. Rafique, S. Bashir, R. Akram, S. Jawaid, M. Bashir, A. Aftab, A. Attique and S. U. Awan, *Ceram. Int.*, 2023, **49**, 5613–5620.
17 M. Z. Ahmad, A. S. Alasiri, J. Ahmad, A. A. Alqahtani, M. M. Abdullah, B. A. Abdel-Wahab, K. Pathak, R. Saikia, A. Das, H. Sarma and S. A. Alzahrani, *Molecules*, 2022, **27**, 7712.
18 L. Harsha, A. Subramanian, N. Balakrishnan and A. Prasad, *J. Complementary Med. Res.*, 2022, **13**, 115.

19 B. K. Mandal, R. Mandal, S. Sikdar, S. Sarma, A. Srinivasan, S. R. Chowdhury, B. Das and R. Das, *Mater. Today Commun.*, 2023, **34**, 105302.

20 K. Velsankar, R. M. Aswin Kumar, R. Preethi, V. Muthulakshami and S. Sudhahar, *J. Environ. Chem. Eng.*, 2020, **8**, 104123.

21 D. Thiruselvi, M. Yuvarani, T. Amudha, R. Sneha, A. K. Mariselvam, M. Anil Kumar, P. Shanmugam and S. Sivanesan, *Energy Sources, Part A*, 2018, **40**, 772–779.

22 A. K. Mittal, Y. Chisti and U. C. Banerjee, *Biotechnol. Adv.*, 2013, **31**, 346–356.

23 A. Surjushe, R. Vasani and D. Saple, *Indian J. Dermatol.*, 2008, **53**, 163.

24 K. Gautam, M. Bhatt, S. Dutt, A. Sagdeo and A. K. Sinha, *Sci. Rep.*, 2025, **15**, 11506.

25 D. Pradhan, S. K. Biswal, N. Nayak, R. Singhal, S. K. Beriha, R. Pattanaik and S. K. Dash, *ChemistrySelect*, 2024, **9**, e202403211.

26 J. Zhang, P. Zhu, Y. Liu, X. Zhu, Y. Li and C.-M. Chen, *J. Energy Storage*, 2025, **112**, 115543.

27 T. Liu, L. Zhang, W. You and J. Yu, *Small*, 2018, **14**, 1702407.

28 J. M. Xu and J. P. Cheng, *J. Alloys Compd.*, 2016, **686**, 753–768.

29 A. Abdisattar, M. Yeleuov, C. Daulbayev, K. Askaruly, A. Tolynbekov, A. Taurbekov and N. Prikhodko, *Electrochem. Commun.*, 2022, **142**, 107373.

30 H.-J. Peng, G.-X. Hao, Z.-H. Chu, Y.-W. Lin, X.-M. Lin and Y.-P. Cai, *RSC Adv.*, 2017, **7**, 34104–34109.

31 C. Bathula, I. Rabani, S. Ramesh, S.-H. Lee, R. R. Palem, A. T. A. Ahmed, H. S. Kim, Y.-S. Seo and H.-S. Kim, *J. Alloys Compd.*, 2021, **887**, 161307.

32 C. R. Babu, A. V. Avani, T. S. Xavier, M. Tomy, S. Shaji and E. I. Anila, *J. Energy Storage*, 2024, **80**, 110382.

33 M. Bhatt, K. Gautam and A. K. Sinha, *Mater. Lett.*, 2025, **389**, 138419.

34 M. Sun, H. Xu, Y. Meng, X.-M. Chen, M. Lu, H. Yu and C.-B. Zhang, *RSC Adv.*, 2022, **12**, 23912–23921.

35 R. Dubey and V. Guruviah, *Ionics*, 2019, **25**, 1419–1445.

36 R. Liang, Y. Du, P. Xiao, J. Cheng, S. Yuan, Y. Chen, J. Yuan and J. Chen, *Nanomaterials*, 2021, **11**, 1248.

37 J. Sun, H. Wang, Y. Li and M. Zhao, *J. Porous Mater.*, 2021, **28**, 889–894.

38 A. N. Naveen and S. Selladurai, *Phys. B*, 2015, **457**, 251–262.

39 R. Ranu, S. L. Kadam, V. K. Gade, S. V. Desarada, M. A. Yewale and K. B. Chavan, *Nanotechnology*, 2024, **35**, 435701.

40 A. Lammini, A. Dehbi, H. Omari, K. ELazhari, S. Mehanned, Y. Bengamra, Y. Dehmani, O. Rachid, A. A. Alrashdi, O. Gotore, A. Abdellaoui and H. Lgaz, *Arabian J. Chem.*, 2022, **15**, 104364.

41 A. N. M. A. Haque, N. Sultana, A. S. M. Sayem and S. A. Smriti, *Sustainability*, 2022, **14**, 11098.

42 S. Salazar Sandoval, A. Amenábar, I. Toledo, N. Silva and P. Contreras, *Sustainability*, 2024, **16**, 1073.

43 A. B. Vennela, D. Mangalaraj, N. Muthukumarasamy, S. Agilan and K. V. Hemalatha, *Int. J. Electrochem. Sci.*, 2019, **14**, 3535–3552.

44 X. Chen, Y. Huan, N. Sun, Y. Su, X. Shen, G. Li, J. Zhang and T. Wei, *Chin. Chem. Lett.*, 2024, **35**, 108380.

45 A. K. Vijh, *Electrochim. Acta*, 1972, **17**, 91–97.

46 S. Saha, M. Jana, P. Khanra, P. Samanta, H. Koo, N. C. Murmu and T. Kuila, *ACS Appl. Mater. Interfaces*, 2015, **7**, 14211–14222.

47 C. G. Van De Walle, *Phys. Status Solidi B*, 2002, **229**, 221–228.

48 N. Wyrsch, F. Finger, T. J. McMahon and M. Vanecek, *J. Non-Cryst. Solids*, 1991, **137–138**, 347–350.

49 P. Makuła, M. Pacia and W. Macyk, *J. Phys. Chem. Lett.*, 2018, **9**, 6814–6817.

50 K. Chatterjee, A. Dutta, S. Mishra, B. Bairy, M. B. Sen, A. Gorai, S. K. Saha and A. J. Akhtar, *Ceram. Int.*, 2023, **49**, 32768–32778.

51 Z. S. Doroudkhani, J. Mazloom and M. M. Ghaziani, *Sci. Rep.*, 2025, **15**, 11436.

52 M. Bhatt, A. K. Sinha, P. Bhojane, M. N. Singh and M. Gupta, *J. Mater. Sci.: Mater. Electron.*, 2023, **34**, 1933.

53 T. Dagar, R. Arya and A. K. Sinha, *Phys. Scr.*, 2025, **100**, 065929.

54 J. Chen, X. Wu and A. Selloni, *Phys. Rev. B: Condens. Matter Mater. Phys.*, 2011, **83**, 245204.

55 P. Parida, R. Kashikar, A. Jena and B. R. K. Nanda, *J. Phys. Chem. Solids*, 2018, **123**, 133–149.

56 S. Kaizaki, in *Instrumental Analysis of Coordination Compounds*, ed. H. Oshio and G. N. Newton, Royal Society of Chemistry, 2024, pp. 1–26.

57 X. Wang, R.-Z. Qiu, Y.-J. Xian, Y.-T. Zhang, P.-C. Liu and P.-C. Zhang, *RSC Adv.*, 2016, **6**, 19150–19154.

58 S. Y. Istomin, O. A. Tyablikov, S. M. Kazakov, E. V. Antipov, A. I. Kurbakov, A. A. Tsirlin, N. Hollmann, Y. Y. Chin, H.-J. Lin, C. T. Chen, A. Tanaka, L. H. Tjeng and Z. Hu, *Dalton Trans.*, 2015, **44**, 10708–10713.

59 H. Singh, H. Ghosh, T. V. Chandrasekhar Rao, A. K. Sinha and P. Rajput, *J. Appl. Phys.*, 2014, **116**, 214106.

60 X. Long, P. Yu, N. Zhang, C. Li, X. Feng, G. Ren, S. Zheng, J. Fu, F. Cheng and X. Liu, *Nanomaterials*, 2019, **9**, 577.

61 R.-P. Wang, M.-J. Huang, A. Hariki, J. Okamoto, H.-Y. Huang, A. Singh, D.-J. Huang, P. Nagel, S. Schuppler, T. Haarman, B. Liu and F. M. F. De Groot, *J. Phys. Chem. C*, 2022, **126**, 8752–8759.

62 Z. Y. Wu, S. Gota, F. Jollet, M. Pollak, M. Gautier-Soyer and C. R. Natoli, *Phys. Rev. B: Condens. Matter Mater. Phys.*, 1997, **55**, 2570–2577.

63 X.-M. Yue, Z.-J. Liu, C.-C. Xiao, M. Ye, Z.-P. Ge, C. Peng, Z.-Y. Gu, J.-S. Zhu and S.-Q. Zhang, *Ionics*, 2021, **27**, 339–349.

64 S. Farid, W. Qiu, J. Zhao, D. Wu, X. Song, S. Ren and C. Hao, *Electrocatalysis*, 2020, **11**, 46–58.

65 K. Xiang, Z. Xu, T. Qu, Z. Tian, Y. Zhang, Y. Wang, M. Xie, X. Guo, W. Ding and X. Guo, *Chem. Commun.*, 2017, **53**, 12410–12413.

66 M. Longhi and L. Formaro, *J. Electroanal. Chem.*, 1999, **464**, 149–157.

67 Y. Jiang and J. Liu, *Energy Environ. Mater.*, 2019, **2**, 30–37.

68 S. Kumar, B. K. Satpathy and D. Pradhan, *Mater. Adv.*, 2024, **5**, 2271–2284.

69 K. Gautam, M. Bhatt, A. Verma and A. K. Sinha, *Biomass Convers. Biorefin.*, 2025, DOI: 10.1007/s13399-025-06799-9.

70 T. Kim, W. Choi, H.-C. Shin, J.-Y. Choi, J. M. Kim, M.-S. Park and W.-S. Yoon, *J. Electrochem. Sci. Technol.*, 2020, **11**, 14–25.

71 S. Kalpana, V. S. Bhat, G. Hegde, T. N. Prabhu and P. N. Anantharamaiah, *Chem. Pap.*, 2024, **78**, 343–356.

72 C. Yang, W. Li, X. Liu, X. Song, H. Li and L. Tan, *Molecules*, 2023, **28**, 3177.

73 R. Lakra, R. Kumar, P. K. Sahoo, D. Sharma, D. Thatoi and A. Soam, *Carbon Trends*, 2022, **7**, 100144.

74 W. Gou, X. Zhou, J. Li and Y. Ma, *Mater. Lett.*, 2016, **180**, 207–211.

75 D. Guo, X. Song, F. Li, L. Tan, H. Ma, L. Zhang and Y. Zhao, *Colloids Surf., A*, 2018, **546**, 1–8.

76 T. Geng, L. Zhang, H. Wang, K. Zhang and X. Zhou, *Bull. Mater. Sci.*, 2015, **38**, 1171–1175.

77 T. Meng, Q.-Q. Xu, Z.-H. Wang, Y.-T. Li, Z.-M. Gao, X.-Y. Xing and T.-Z. Ren, *Electrochim. Acta*, 2015, **180**, 104–111.

78 M. Gopalakrishnan, G. Srikesh, A. Mohan and V. Arivazhagan, *Appl. Surf. Sci.*, 2017, **403**, 578–583.

79 L. Tao, L. Shengjun, Z. Bowen, W. Bei, N. Dayong, C. Zeng, Y. Ying, W. Ning and Z. Weifeng, *Nanoscale Res. Lett.*, 2015, **10**, 208.

80 W. Wang, Y. Yuan, J. Yang, L. Meng, H. Tang, Y. Zeng, Z. Ye and J. Lu, *J. Mater. Sci.*, 2018, **53**, 6116–6123.

81 C. T. Anuradha and P. Raji, *Appl. Phys. A*, 2020, **126**, 164.

82 I. Shaheen and K. S. Ahmad, *J. Mater. Sci.: Mater. Electron.*, 2020, **31**, 10323–10333.

83 E. Dai, J. Xu, J. Qiu, S. Liu, P. Chen and Y. Liu, *Sci. Rep.*, 2017, **7**, 12588.

84 T. Liu, L. Zhang, W. You and J. Yu, *Small*, 2018, **14**, 1702407.

85 P. Sheng, S. Tao, X. Gao, Y. Tan, D. Wu, B. Qian and P. K. Chu, *J. Mater. Sci.*, 2020, **55**, 12091–12102.

86 X. Wang, H. Xia, X. Wang, J. Gao, B. Shi and Y. Fang, *J. Alloys Compd.*, 2016, **686**, 969–975.

87 M. Qorbani, N. Naseri and A. Z. Moshfegh, *ACS Appl. Mater. Interfaces*, 2015, **7**, 11172–11179.

88 P. M. Kharade, J. V. Thombare, A. R. Babar, R. N. Bulakhe, S. B. Kulkarni and D. J. Salunkhe, *J. Phys. Chem. Solids*, 2018, **120**, 207–210.

89 L. Zhang, H. Zhang, X. Chu and X. Han, *Ionics*, 2019, **25**, 5445–5458.

90 E. Duraisamy, H. T. Das, A. Selva Sharma and P. Elumalai, *New J. Chem.*, 2018, **42**, 6114–6124.

91 S. Yan, L. Xu, J. Jiang, H. Xiao and X. Li, *J. Alloys Compd.*, 2018, **764**, 684–690.